small ϵ, δ while the energy which resides in the stretched ridge[8] is $U_s = E_b\epsilon^{7/3}(2D/h)^{1/3}$, so that $U_s/U_b \approx 0.05$ for typical experimental parameters. These results indicate that in the early stages of crumpling, when large deformations of a few conical dislocations are much more likely to occur, bending dominates stretching. Finally, by continuing the computation of the $F - \epsilon$ curve beyond the experimentally accessible parameters, we see the appearance of a snap-through instability similar to that for a single dislocation.

A series of such events (that is, geometric softening—dynamic snap-through—local topological stiffening) provides us with a microscopic mechanism for the crumpling of a large thin elastic sheet. As the sheet is deformed by a force, it forms a developable cone that deforms, softens and eventually becomes dynamically unstable, and an acoustic pulse is emitted when the sheet pops into a folded configuration. This stiffens the sheet locally, but soon new developable cones (and stretched ridges which connect them) begin to form. Ridges may buckle in two ways. (1) In the plane of the ridge by forming a developable cone about which the ridge pivots and folds, locally leading to roughly the same scenario as that for a single conical dislocation, or (2) in a direction perpendicular to the ridge by forming two dislocations that move apart along a new ridge about which the original ridge folds, as seen during the bending of a drinking straw. A cascade of these instabilities on ever-decreasing length scales leads to the formation of new conical dislocations as the sheet crumples, and the energy of deformation is pumped down to smaller and smaller scales. As the size of these folds becomes smaller, the incremental deformation is concomitantly less, and a cross-over to the regime where stretching and bending deformations are of the same order is likely[8]. However any analysis of this stage in crumpling must also account for inelastic deformations. On length scales much larger than the thickness but much smaller than the length or breadth of the sheet, these dynamical snap-throughs constitute a self-similar cascade and are accompanied by acoustic emissions. While preliminary experiments[17,18] are suggestive of power-law behaviour for the statistics of these sounds, they remain incompletely quantified: much work remains to be done in this area. □

Received 1 February; accepted 17 June 1999.

1. Calladine, C. *Theory of Shell Structures* (Cambridge Univ. Press, Cambridge, 1983).
2. Wierzbicki, T. & Jones, N. (eds) *Structural Failure* (Wiley Interscience, New York, 1988).
3. Connelly, R. Rigidity and energy. *Invent. Math.* **66,** 11–33 (1982).
4. Nelson, D. R., Piran, T. & Weinberg, S. *Statistical Mechanics of Membranes and Surfaces* (World Scientific, Singapore, 1988).
5. Amirbayat, J. & Hearle, J. W. S. The complex buckling of flexible sheet materials. *Int. J. Mech. Sci.* **28,** 339–370 (1986).
6. da Vinci, Leonardo *Notebooks* Vol. I., *Studies of Drapery* (Dover Reprint, New York, 1984).
7. Rayleigh, Lord, *Theory of Sound* Vol. I, Ch. X a (Dover, New York, 1945).
8. Lobkovsky, A., Gentges, S., Li, H., Morse, D. & Witten, T. Stretched ridges in crumpling. *Science* **270,** 1482–1485 (1995).
9. Lobkovsky, A. & Witten, T. A. Properties of ridges in elastic membranes. *Phys. Rev. E* **55,** 1577–1589 (1997).
10. Chaieb, S. & Melo, F. Experimental study of developable cones. *Phys. Rev. Lett.* **80,** 2354–2357 (1998).
11. Cerda, E. & Mahadevan, L. Conical surfaces and crescent singularities in crumpled sheets. *Phys. Rev. Lett.* **80,** 2358–2361 (1998).
12. Ben Amar, M. & Pomeau, Y. Crumpled paper. *Proc. R. Soc. Lond. A* **453,** 729–755 (1997).
13. Nabarro, F. R. N. *Theory of Crystal Dislocations* (Dover, New York, 1993).
14. Struik, D. J. *Lectures on Classical Differential Geometry* (Dover, New York, 1988).
15. Love, A. E. H. *A Treatise on the Mathematical Theory of Elasticity* (Dover, New York, 1944).
16. Timoshenko, S. & Gere, J. *Theory of Elastic Stability* (McGraw-Hill, New York, 1961).
17. Kramer, E. & Lobkovsky, A. Universal power law in the noise from a crumpled elastic sheet. *Phys. Rev. E* **53,** 1465–1468 (1996).
18. Houle, P. & Sethna, J. Acoustic emission from crumpling paper. *Phys. Rev. E* **54,** 278–283 (1996).

Acknowledgements

E.C. was supported by the Chilean Presidente de la República postdoctoral fellowship during the course of this work at MIT in 1997–98. S.C. was supported by a postdoctoral fellowship at Universidad de Santiago de Chile in 1997–98 during the course of this work. Additional support was provided by the Chilean Cátedra Presidencial en Ciencias (F.M.), the Karl van Tassel career development chair and the Sloan fund (L.M.) at MIT.

Correspondence and requests for materials should be addressed to L.M. (l_m@mit.edu).

Direct observation of *d*-orbital holes and Cu–Cu bonding in Cu_2O

J. M. Zuo*, M. Kim*, M. O'Keeffe† & J. C. H. Spence*

* *Department of Physics and Astronomy,* † *Department of Chemistry, Arizona State University, Tempe, Arizona 85287, USA*

A striking feature of metal oxide chemistry is the unusual electronic and chemical behaviour of Cu(I) and Ag(I): a case in point is that detailed understanding of Cu–O bonding is essential to the theory of high-temperature copper oxide superconductors. Both cations are usually coordinated in a linear fashion to two oxygens, particularly for Cu(I). In many compounds, the Cu(I) and Ag(I) cations also adopt close-packed (and related) configurations with short metal–metal distances that are strongly suggestive of the occurrence of metal–metal bonding[1,2] despite their formal nd^{10} configuration. Such observations have been explained[3,4] by invoking the participation in bonding of electronic orbitals of higher principal quantum number—that is, $(n+1)s$ and $(n+1)p$—accompanied by the creation of *d*-orbital holes on the metal ion. To test this hypothesis, we have used a recently developed method of quantitative convergent-beam electron diffraction[5] combined with X-ray diffraction to map the charge-density distribution in the simple oxide Cu_2O, the results of which we then compare with electronic-structure calculations. We are able to image directly the *d* holes on the copper atoms, and also demonstrate the existence of Cu–Cu bonding in this compound.

Cu_2O has a cubic structure with no free internal parameters (only Ag_2O is isostructural). The copper atoms are at the points of a face-centred-cubic lattice, with oxygen atoms in tetrahedral sites at positions (1/4,1/4,1/4) and (3/4,3/4,3/4) of the cubic cell. The resulting arrangement of Cu–O links is made up of two interpenetrating networks (Fig. 1). The simplest description of Cu_2O using an ionic model with closed-shell (spherical) Cu^+ and O^{2-} ions is known to be inadequate. Not only does it fail to explain the observed linear 2-coordination of Cu but also it is not in accord with the observation that the two sublattices repel each other electrostatically, so that to account for their interpenetration some short-range Cu–Cu attractive interaction must be invoked[6]. We note that the closest approach of atoms of the two networks is a Cu–Cu distance of 3.02 Å—the shortest O–O distances are 3.70 Å.

Considerable progress has been made in mapping the charge density of light-element molecular crystals by X-ray diffraction[7], especially using a synchrotron source[8]. The extension of this method

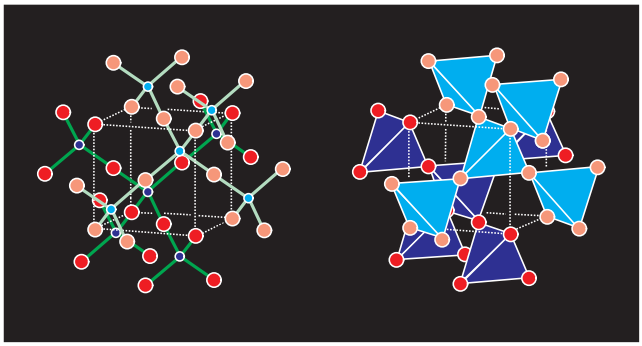

Figure 1 The structure of Cu_2O. Left, as a ball and stick model with O atoms blue, Cu atoms red and bonds green. One network is coloured darker than the other. Note that there are no bonds joining the two nets. Right, as corner-connected OCu_4 tetrahedra. Dark and light tetrahedra are on independent networks. In both sketches, dotted white lines outline a unit cell.

to inorganic solids of interest to material science is complicated by the X-ray extinction effect, which masks the much smaller bonding effect at low scattering angles, especially for heavy elements[9]. The electron-diffraction method used here allows the extinction-free measurement of low-order crystal structure factors, which are most sensitive to valence electrons. Following an earlier suggestion[10], we combine these structure factors with X-ray diffraction results for weak and high-order reflections. Electron diffraction was also used to assess the error due to extinction in X-ray diffraction data, and to replace strongly affected reflections with electron-diffraction data. The result clearly shows that ambiguities in previous X-ray studies[11,12] of the charge density of Cu_2O (cuprite) are due to large extinction effects on the strong low-order reflections.

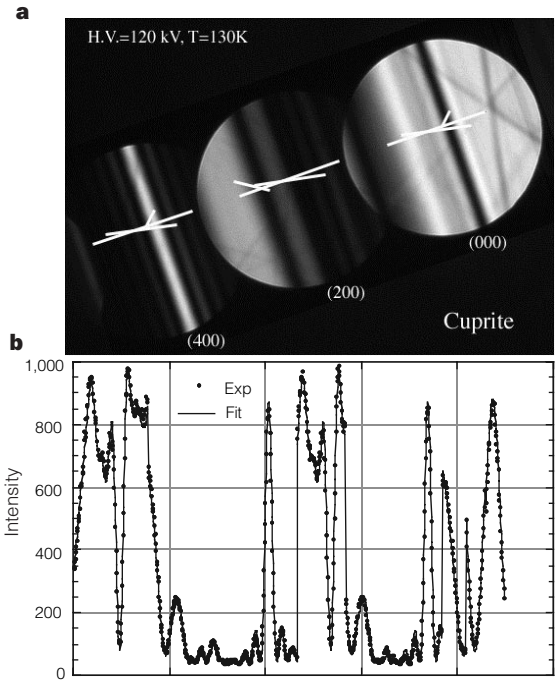

Figure 2 An example of electron diffraction structure factor measurement for Cu_2O (200) and (400). **a**, Experimentally recorded and processed CBED pattern; **b**, best fit for points along lines indicated in **a**, displayed sequentially along the *x*-axis and with the recorded intensity on the *y*-axis in counts. The experiment was performed using an LEO-912 Ω energy-filtering electron microscope with a Gatan liquid-nitrogen-cooled sample holder. The specimen used is a natural Cu_2O (cuprite) cooled to ~130 K. A 15-eV energy-filtering slit was placed around the zero-loss peak to remove the contribution from inelastically scattered electrons, which form a background due to plasmon and other loss processes. Off-zone-axis systematic diffraction conditions were used to collect diffraction intensities for reflections up to (400). The CBED patterns were recorded on both a slow-scan CCD camera and on Fuji imaging plates, which were then processed for fitting[5]. The refinement was carried out using the EXTAL program[5].

Accurate measurements of the low-order structure factors were made with a versatile, quantitative, convergent-beam electron diffraction (CBED) technique[5] that we have developed recently. The method takes advantage of the small probe (of nanometre dimensions) available in our electron microscope. Using this probe, one can almost always find a region of perfect crystals, for which the perfect-crystal theory of dynamical diffraction can be applied. The measurements are made by comparing experimental intensity profiles across CBED disks (rocking curves) with calculations, using a goodness of fit (GOF) criterion, as illustrated in Fig. 2. The intensity is calculated using the Bloch wave method, with structure factors, absorption coefficients, the beam direction and thickness treated as refinable parameters. Structure factors for the (531) and higher-order reflections out to (14,4,2) were taken from X-ray measurements[11]. Weak (odd, even) and very weak (even, even, odd) reflections—except (110)—were also taken from X-ray work.

Multipole refinement[7,13] provides the most efficient parametrization of real space charge density, and gives a result which is insensitive to the missing reflections in the collected data set[11]. In this method, the crystal charge density is fitted by a sum of non-spherical pseudo-atomic densities. These consist of a spherical-atom (or ion) charge density obtained from multi-configuration Dirac-Fock calculations[14] with variable orbital occupation factors to allow for charge transfer, and a small non-spherical part in which local symmetry-adapted spherical harmonic functions were used. In addition, atomic vibrations were accounted for using the Charlier–Gram expansion[7] for the temperature factor; as the electron and X-ray measurements were done at different temperatures, the combined refinement used the almost linear dependence of temperature factors between 100 and 300 K (ref. 12). Refinements with, and without, anharmonic terms in the temperature factor clearly show the importance of an anharmonic term for Cu, especially for high-order reflections with $s = \sin\theta/\lambda > 1.0$ Å^{-1}. In either case the charge transfer from Cu to O refined to 1.01(5); that is, Cu^+ and O^{2-}.

Compared to previous results[11,12], we obtain much better estimates for the non-spherical distortion of O and Cu. This improvement is due to the absence of extinction effects in our electron-diffraction measurements. X-ray diffraction has a particularly strong extinction effect for strong reflections with small *s* values. For example, for Cu_2O(200), the X-ray structure factor $F^X \approx 78.8$ electrons per cell, and the measured value by X-ray diffraction is

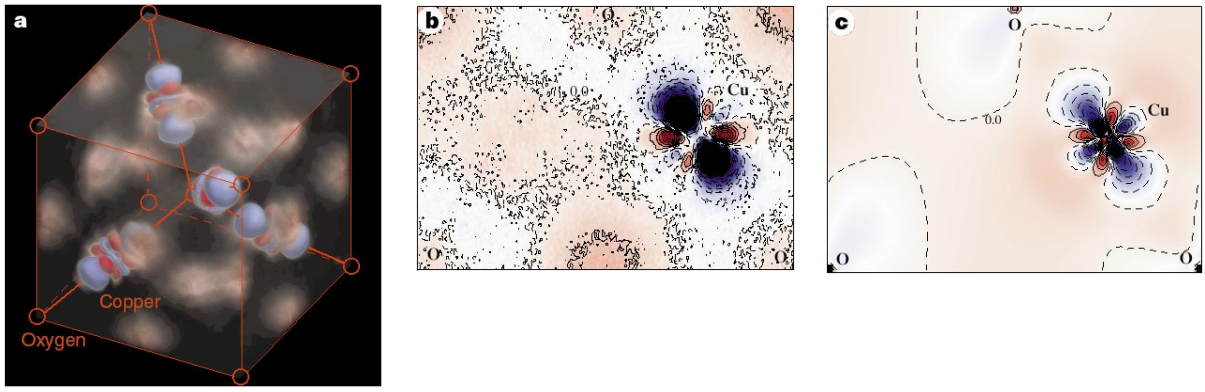

Figure 3 The experimental and theoretical difference maps between the static crystal charge density and superimposed spherical O^{2-} and Cu^+ ions. **a**, A three-dimensional rendering of the experimental difference map from the multipole model fitting with anharmonic temperature factors. The map was made using the T3D program (Fortner Research, USA) using a colour scheme of blue ($\Delta\rho < 0$), white ($\Delta\rho = 0$) and red ($\Delta\rho > 0$). A translucency factor was used to remove the mostly white background. **b**, Contour map of the difference charge density in a (110) plane with a contour increment of 0.2 electrons per Å^2 and coloured using the same colour scheme as in **a**. The dashed line is for contours with $\Delta\rho \leq 0$. **c**, The difference charge density map obtained from the FLAPW (LDA) calculations, plotted in the same way as **b**.

about 90% of the actual value, with a difference of ~7.9 electrons per cell. For this reflection, the difference between the ionic and the neutral-atom models is about 0.07 electrons per cell. To detect this very small difference, the extinction correction used has to have better than 1% accuracy. By comparison, the electron-diffraction measurement has an accuracy of 0.04 electrons per cell. The electron measurements allow us to evaluate the extinction effect in the X-ray data and exclude those with a large extinction factor.

The large non-spherical contributions in the multipole fitting point to an appropriate description of the charge density in terms of distorted ions; the effect of covalent bonding interactions (that is, interactions other than the electrostatic between spherical ions) can be seen by comparing the 'measured' (multipole refinement) electron density with that resulting from a model consisting of superposition of spherical ions. In Fig. 3a we show a three-dimensional plot of the difference between the static crystal charge density (obtained from the multipole fitting to experiment) and the superimposed charge density of spherical O^{2-} and Cu^{+} ions calculated by the multi-configuration Dirac–Fock method. The charge density of the O^{2-} ion was calculated using a Watson sphere of 1.2 Å radius; this is the value that gives the best fit to experiment within the limitation of a spherical ion model. Figure 3b shows a contour map of the difference charge density for the (110) plane; this was synthesized by introducing random noise to the Fourier coefficients for each pixel, to illustrate the uncertainty in the mapped charge density. The noise introduced reflects the uncertainty in the estimated multipole parameters. For comparison, in Fig. 3c, we also plot the theoretical difference charge density map obtained from the full potential linearized augmented plane wave (FLAPW) method, using the local density approximation (LDA) for exchange and correlation and the WIEN95 program[15] (this is an updated version of the program in ref. 16). This calculation improves on the previous calculation[17] using the muffin-tin potential approximation. For the theoretical map, the charge densities of O^{2-} and Cu^{+} ($3d^{10}$) ions were calculated using the same LDA as the FLAPW calculation.

The electron density difference shown in Fig. 3a would be zero everywhere if cuprite were purely ionic (that is, if it consisted of spherical ions). The difference, here seen unambiguously for the first time (to our knowledge), confirms earlier theoretical speculation[1–4] that a covalent contribution exists. The correspondence between our experimental map and the classical diagrams of d_z^2 orbitals sketched in textbooks is striking. All our difference maps show strong non-spherical charge distortion around the copper atoms, with the characteristic shape of *d* orbitals, and excess charge in the interstitial region. There is little variation around oxygen in both the experimental and the theoretical results, which suggests that an O^{2-} anion description is valid. The most significant difference between experiment and theory is around Cu, and the charge in the interstitial region. The charge modification around Cu in the experiment is broader and larger than the theory. The experimental map also shows a large (~0.2 electrons per $Å^3$) positive peak in the unoccupied tetrahedral interstitial region of the four neighbouring Cu atoms, which suggests a strong Cu^{+}–Cu^{+} covalent bonding. For comparison, the Si–Si covalent bond peak is about 0.21 electrons per $Å^3$ (ref. 18). We note that these differences between experiment and theory are experimentally significant. In Fig. 4, we compare experimental and theoretical structure factors. The experiment structure factor clearly shows a large deviation from that of superimposed neutral atoms. The difference between theory and experiment is generally larger than the experimental error.

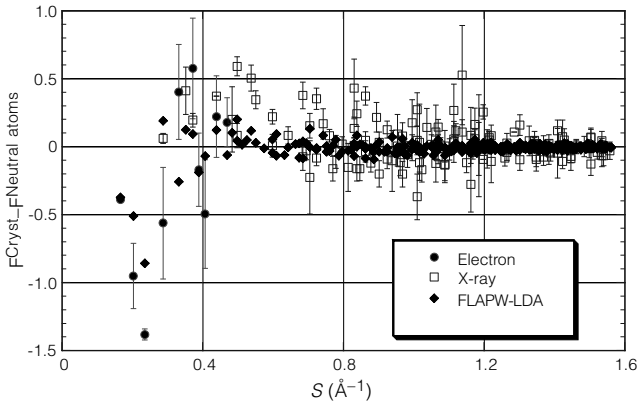

Figure 4 Comparison between experimental and theoretical structure factors (*F*). The structure factor shown is the difference between the crystal and the neutral atoms model. The error bar of first reflection is smaller than the circle.

The non-spherical charge density around Cu^{+} can be interpreted as being due to the hybridization of *d* electrons with higher-energy unoccupied *s* and *p* states[3,4,17]. Among these states, hybridization is only allowed for d_z^2 and 4*s* by symmetry, and when this happens part of the d_z^2 state becomes unoccupied (a *d*-orbital hole). These states are responsible for the spatial distribution of the deficiency in the map shown in Fig. 3a. The complementary empty states are important for spectroscopies which probe empty states, such as electron energy-loss spectroscopy and X-ray absorption spectroscopy[19]. The experimental studies reveal that the unoccupied states are predominately Cu-*d* character for the Cu $L_{2,3}$ edge; theory shows that they originate from hybridized d_z^2 orbitals. This theoretical interpretation, based on the calculated partial density of states of the one-electron band structure, is supported by the generally good agreement with experimental spectroscopy of both occupied and unoccupied states[19]. From the characteristic and localized distortion around Cu, we can estimate the population of the outer valence shells from the multipole model coefficients[7,11]. From the data in Table 1, we estimate the hybridization coefficient, $|x|$, between d_z^2 and 4*s* to be 0.36, so that about 0.22 electrons per atom are removed from d_z^2 states. This is in good agreement with the calculated density of states, which gives a similar number for *x*. □

Received 12 March; accepted 16 July 1999.

1. Jansen, M. Homoatomic d^{10}-d^{10} interactions: their effects on structure and chemical and physical properties. *Angew. Chem. Int. Edn. Engl.* **26,** 1098–1110 (1987).
2. Pyykkö, P. Strong closed-shell interactions in inorganic chemistry. *Chem. Rev.* **97,** 597–636 (1997).
3. Orgel, L. E. Stereochemistry of metals of the B sub-group. Part I, ions with filled d-electron shells. *J. Chem. Soc.* 4186–4190 (1958).
4. Merz, K. M. & Hoffman, R. d^{10}-d^{10} interactions: multinuclear copper(I) complexes. *Inorg. Chem.* **27,** 2120–2127 (1988).

Table 1 Cu_2O multipole model refinement results

O			Cu				q (*e*)	R (%)
α ($Å^{-1}$)	P_{oct}	P_{hex}	α ($Å^{-1}$)	P_{20}	P_{40}	P_{43+}		
2.24 (10)	–1.65 (14)	3.28 (10)	15.7(10)	–0.195 (30)	–0.219 (38)	–0.043 (20)	1.01 (5)	0.71

In the multipole model, crystal charge density is a sum of aspherical 'atoms'[16]: $\rho^a(\mathbf{r}) = \rho^s(\mathbf{r}) + \Sigma_{lm\pm} P_{lm\pm} N_{lm\pm} R_l(r) y_{lm\pm}(\theta\phi)$. Here ρ^s is the spherical charge with $\rho^s_{Cu} = \rho^s_{Cu^+} + (1-q)(\rho^s_{Cu} - \rho^s_{Cu^+})$, and $\rho^s_O = \rho^s_O + q(\rho^s_{O^{2-}} - \rho^s_O)$ with *q* as the charge transfer from Cu to O; $R_l(r) = r^{n_l} \exp(-\alpha r)$ ($n_3 = 3$; $n_4 = 4$) is the radial function with population coefficient $P_{lm\pm}$; $N_{lm\pm}$ is the density-normalization coefficient. Numbers in parentheses are estimated standard deviations.

5. Zuo, J. M. Quantitative convergent beam electron diffraction. *Mater. Trans. JIM* **39,** 938–946 (1998).
6. O'Keeffe, M. Madelung constants for the C3 and C9 structures. *J. Chem. Phys.* **38,** 3035–3038 (1963).
7. Coppens, P. *X-ray Charge Densities and Chemical Bonding* (Oxford, New York, 1997).
8. Koritsanszky, T. *et al.* Accurate experimental electronic properties of DL-proline monohydrate obtained within 1 day. *Science* **279,** 356–358 (1998).
9. Stewart, R. F. & Spackman, M. in *Structure and Bonding in Crystals* (eds O'Keeffe, M. & Navrotsky, A.) 279–298 (Academic, New York, 1981).
10. Smart, D. J. & Humphreys, C. J. The application of electron diffraction to determining bonding charge densities in crystals. *Int. Phys. Conf. Ser.* **52,** 211–214 (1980).
11. Restori, R. & Schwarzenbach, D. Charge density in cuprite, Cu_2O. *Acta Crystallogr. B* **42,** 201–208 (1986).
12. Kirfel, A. & Eichhorn, K. Accurate structure analysis with synchrotron radiation, the electron density in Al_2O_3 and Cu_2O. *Acta Crystallogr. A* **46,** 271–284 (1990).
13. Stewart, R. F. Electron population analysis with rigid pseudoatoms. *Acta Crystallogr. A* **32,** 565–574 (1976).
14. Rez, D., Rez, P. & Grant, I. Dirac-Fock calculations of X-ray-scattering factors and contributions to the mean inner potential for electron-scattering. *Acta Crystallogr. A* **50,** 481–497 (1994); correction **53,** 522 (1997).
15. Blaha, P., Schwarz, K. & Luitz, J. WIEN97 (Vienna Univ. of Technol., Vienna, 1997).
16. Blaha, P., Schwarz, K., Sorantin, P. & Trickey, S. B. Full-potential, linearized augmented plane-wave programs for crystalline systems. *Comput. Phys. Commun.* **59,** 399–415 (1990).
17. Marksteiner, P., Blaha, P. & Schwarz, K. Electronic structure and binding mechanism of Cu_2O. *Z. Phys. B* **64,** 119–127 (1986).
18. Zuo, J. M., Blaha, P. & Schwarz, K. The theoretical charge density of silicon: experimental test of exchange and correlation potentials. *J. Phys. Condens. Matt.* **9,** 7541–7561 (1997).
19. Ghijsen, J. *et al.* Electronic structure of Cu_2O and CuO. *Phys. Rev. B* **38,** 11322–11330 (1988).

Acknowledgements

We thank A. Avilov for discussions, and D. Schwarzenbach for providing the X-ray data. This work was supported by the NSF.

Correspondence and requests for materials should be addressed to J.M.Z. (e-mail: Zuo@asu.edu).

Discerning vibronic molecular dynamics using time-resolved photoelectron spectroscopy

Valérie Blanchet, Marek Z. Zgierski, Tamar Seideman & Albert Stolow

Steacie Institute for Molecular Sciences, National Research Council of Canada, Ottawa, Ontario, Canada K1A 0R6

Dynamic processes at the molecular level occur on ultrafast time scales and are often associated with structural as well as electronic changes. These can in principle be studied by time-resolved scattering[1–3] and spectroscopic methods, respectively. In polyatomic molecules, however, excitation results in the rapid mixing of vibrational and electronic motions, which induces both charge redistribution and energy flow in the molecule[4,5]. This 'vibronic' or 'non-adiabatic' coupling is a key step in photochemical[6] and photobiological processes[7] and underlies many of the concepts of molecular electronics[8], but it obscures the notion of distinct and readily observable vibrational and electronic states. Here we report time-resolved photoelectron spectroscopy measurements that distinguish vibrational dynamics from the coupled electronic population dynamics, associated with the photo-induced internal conversion, in a linear unsaturated hydrocarbon chain. The vibrational resolution of our photoelectron spectra allows for a direct observation of the underlying nuclear dynamics, demonstrating that it is possible to obtain detailed insights into ultrafast non-adiabatic processes.

The Born-Oppenheimer approximation (BOA), an adiabatic separation of electronic from nuclear motions, has the pivotal role in defining the potential energy surface and thus permits a mechanistic picture of molecular dynamics. The breakdown of the BOA is due to the motions of the atoms near the intersections of potential surfaces belonging to different electronic states. This mixing of vibrational and electronic motions in excited molecules can in principle be inferred from both frequency-resolved and time-resolved optical spectroscopies. Time-resolved experiments may be generally understood as preparing an excited state with a pump pulse and then, as a function of time, projecting it with a probe pulse onto a final state which acts as a template[9–17]. Ideally, the final state should be well characterized. Photoionization detection has several conceptual and practical advantages[10]. The ion state may be well characterized by independent methods such as high resolution photoelectron spectroscopy and *ab initio* computation. Photoelectron detection has the additional advantage that the signal may be dispersed with respect to kinetic energy and angular distribution. Photoelectron spectroscopy has, compared with optical spectroscopies, fairly relaxed selection rules: any molecular state can be ionized (no 'dark' states). A simplified but very useful picture is that emission of an independent outer electron can occur without the simultaneous electronic reorganization of the ion core (Koopmans' approximation). Partial photoionization probabilities can differ drastically with respect to the molecular orbital nature of the neutral electronic state. If a given electronic configuration correlates—upon removal of the outermost electron—to the electronic configuration of the ground electronic state of the cation, then the corresponding photoionization probability is much higher than if it does not.

Time-resolved photoelectron spectroscopy (TRPES) has been proposed as a technique for the study of ultrafast non-adiabatic processes[10–14] and spin–orbit coupling[15] in isolated polyatomic molecules. The TRPES method has been shown to provide details

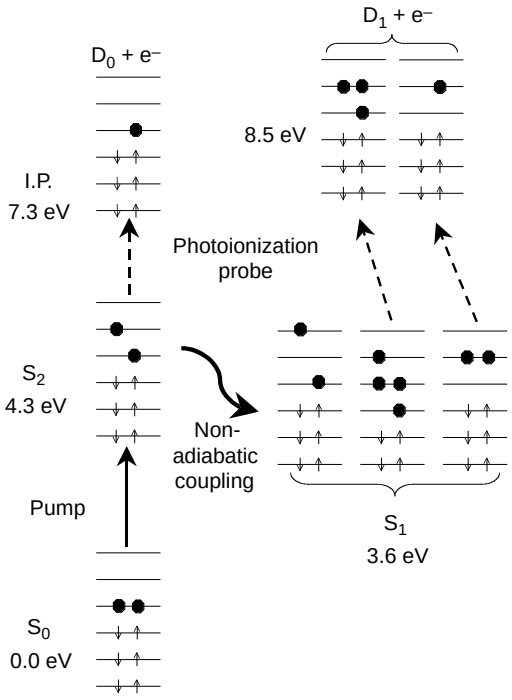

Figure 1 Molecular orbital configurations and photoionization correlations in all-*trans* 2,4,6,8 decatetraene, DT. The optically coupled S_2 (excitation at 4.3 eV shown by straight solid arrow) state is a singly excited configuration, whereas the lower-lying optically forbidden S_1 (3.6 eV) state is composed of both singly and doubly excited configurations. The curved solid arrow indicates non-adiabatic coupling in the excited state. On removal of the highest-lying electron, S_2 correlates with the D_0 cation ground-state configuration with an ionization potential (I.P.) of 7.3 eV, whereas S_1 correlates predominantly with the D_1 cation excited-state configurations at 8.5 eV. it is therefore expected, assuming a single active electron, that the photoionization electronic channel should switch from $D_0 + e^-$ to $D_1 + e^-$ during the $S_2 \rightarrow S_1$ internal conversion. The dashed arrows indicate the most probable ionization channels.